High-order harmonics generation in nanosecond-pulses-induced plasma containing Ni-doped $CsPbBr_3$ perovskite nanocrystals using chirp-free and chirped femtosecond pulses

To cite this article: Srinivasa Rao Konda *et al* 2023 *Nanotechnology* **34** 055705

IOP Publishing Nanotechnology
Nanotechnology 34 (2023) 055705 (13pp) https://doi.org/10.1088/1361-6528/ac9fdb

High-order harmonics generation in nanosecond-pulses-induced plasma containing Ni-doped $CsPbBr_3$ perovskite nanocrystals using chirp-free and chirped femtosecond pulses

Srinivasa Rao Konda[1,*], Rashid A Ganeev[2,3,4], Vyacheslav V Kim[2], Ravi Ketavath[5], Jiaqi Yu[1] and Wei Li[1,*]

[1] GPL photonics laboratory, State Key Laboratory of Applied Optics, Changchun Institute of Optics, Fine Mechanics and Physics, Chinese Academy of Sciences, Changchun 130033, People's Republic of China
[2] Laboratory of Nonlinear Optics, Institute of Astronomy, University of Latvia, Jelgavas iela 3, Riga, LV—1004, Latvia
[3] Tashkent Institute of Irrigation and Agricultural Mechanization Engineers, National Research University, Kori Niyazov street 39, Tashkent 100000, Uzbekistan
[4] Department of Physics, Voronezh State University, Voronezh 394006, Russia
[5] Solar Cells and Photonics Research Laboratory, School of Chemistry, University of Hyderabad, Hyderabad 500046, Telangana, India

E-mail: ksrao@ciomp.ac.cn and weili1@ciomp.ac.cn

Received 31 August 2022, revised 27 October 2022
Accepted for publication 2 November 2022
Published 18 November 2022

Abstract

We demonstrate high-order harmonic generation in Ni-doped $CsPbBr_3$ perovskite nanocrystals ablated by nanosecond pulses using chirp-free 35 fs, and chirped 135 fs pulses in the case of single-color pump (800 nm) and a two-color pump (800 and 400 nm). We analyzed the spectral shift, cut-off, and intensity distribution of harmonics in the case of chirped drving pulses compared to chirp-free pulses. It is shown that the presence of Ni dopants and $CsPbBr_3$ plasma components improves the harmonics emission. Also, we measured the third-order nonlinear optical (NLO) properties of these nanocrystals using 800 nm, 60 fs, 1 kHz pulses. The variations of measured NLO parameters of $CsPbBr_3$ perovskite nanocrystals containing different concentrations of nickel correlate with variations of generated high-order harmonics from laser induced plasmas of studied nanocrystals in terms of harmonics intensity, cut-off, and spectral shift (in case of chirped driving pulses). The spectral shift of the harmonics generated from the Ni-doped $CsPbBr_3$ perovskite nanocrystals can be used to form tunable extreme ultraviolet sources.

Keywords: Ni-doped $CsPbBr_3$, 2D nanocrystals, perovskites, high-order harmonics, nanosecond pulses, laser-induced plasma

(Some figures may appear in colour only in the online journal)

1. Introduction

High-order harmonics generation (HHG) from laser-induced plasmas (LIPs) has widely attracted for researchers attention to develop tunable extreme ultraviolet (XUV) sources due to the availability and synthesis of numerous solid materials. To date, gases have been widely used as medium sources for HHG [1–3]. Due to the limited types of elements in gas states in nature, the research on HHG experiments using gases is greatly limited. Therefore, in addition to gaseous substances, researchers

* Authors to whom any correspondence should be addressed.

have also tried substances in other states, including solid, liquid, etc. However, due to the damage threshold of the solid, the laser intensity used in the experiment is limited. In this way, the photon energy obtained is not very high. The meta-photonic platforms may overcome this shortage. With a plasmon-enhanced metasurface or the structure surface with a high refractive index of dielectric resonator [4, 5], meta-photonic platforms enable the observation of higher harmonic orders enhanced harmonic yields. The generation of high-order harmonics from the liquid is restricted to difficult to control in the vacuum; this experiment needs high-precision equipment to produce an ultra-thin liquid jet in a vacuum. Therefore, in the current work, we employ the method of LIPs to generate harmonics. The use of LIPs could greatly broaden the choices of atomic species because this method can be applied to almost any material surface, which is helpful to effectively generate and optimize harmonics by exploring the nonlinear characteristics of different materials. Moreover, the HHG from LIPs of several different metals [6, 7] shows strong resonance enhancement, which may be used to improve harmonic conversion efficiency.

In the present work, we have chosen undoped and Ni-doped $CsPbBr_3$ nanocrystal LIPs for the efficient medium for tunable higher-order harmonics. Halide perovskite nanocrystals, nanocomposites, quantum dots, single crystals, and thin films are some of the research spotlights in optoelectronics and photonics [8–18]. Recently, $CsPbBr_3$ perovskites nanocrystals attracted the great attention of researchers due to their promising applications in lasers, light-emitting diodes, photodetectors, and photodiodes. Apart from various shapes of pure $CsPbBr_3$, doping with other substances significantly improved their optical properties. For example, several research groups explored the various applications of doped $CsPbBr_3$ perovskites, such as a brand-new architecture design of $CsPbBr_3$-glass nanocomposite on the sapphire plate was proposed for laser-driven projection display [19], applications of stable zirconia-coated and crystallization dynamics of $CsPbBr_3$ nanocrystals in light-emitting diodes and luminescence properties [20, 21]. Lasing performance was significantly improved by ZnO nanoparticle-decorated highly compact $CsPbBr_3$ perovskite thin films [22]. Furthermore, ligand-modified $CsPbBr_3$ quantum dots [23] and SiO_2 spheres embedded on $CsPbBr_3$ quantum dots [24] led to enhanced amplified spontaneous emission, produced highly effective emission and warm white light-emitting diodes with a high color rendering index along with producing stable and low-threshold whispering-gallery-mode lasing [25]. Similarly, various lanthanide ions in the lattices of $CsPbCl_3$ perovskite nanocrystals possess high photoluminescence quantum yield and emit widely tunable multicolor radiations [26]. Zhou *et al* reported Ag-doped $CsPbBr_3$ nanocrystals with the tunable band structure and efficient charge transport [27]. Yong *et al* performed the density functional theory calculations. They revealed that Ni doping of perovskites lead to the growth of defect formation energy and does not introduce deep trap states in the band gap, which is the main reason for the improved local structural order and near-unity photoluminescent quantum yield [28]. Thus, the works mentioned above indicate that the doped perovskite nanocrystals will inherit most of the unique optical properties compared to the undoped nanocrystals. Here, we chose the Ni-doped $CsPbBr_3$ 2D colloidal nanocrystals for the emission of higher-order harmonics. However, based on earlier studies, Ni-doping $CsPbBr_3$ nanocrystals demonstrated outstanding nonlinear optical (NLO) properties [28, 29]. The synthesis, optical, and morphological properties of undoped $CsPbBr_3$ and Ni-doped $CsPbBr_3$ 2D colloidal nanocrystals are reported elsewhere [29]. Our earlier studies revealed that Ni-$CsPbBr_3$ nanocrystals have a massive impact on the emission of higher-order harmonics. In that case, we ablated the perovskite nanocrystals by picoseconds pulses and measured the harmonic spectra for chirp-free and chirped driving pulses (DP) [30, 31].

Meanwhile, plasma characteristics significantly differ with the duration of ablating laser pulse, leading to variations in absorption, heating, and ablation [32–36]. The spatio-temporal distribution of plasma produced by long laser pulses differs from that produced by short laser pulses [37–39]. Therefore, in the present work, we have extended our investigation on the effect of emission of higher-order harmonics from the nanocrystal plasma produced by nanosecond pulses using chirp-free and chirped DP at fixed delays. Additionally, we correlated the intensity and cut-off of harmonics enhancement with third-order NLO properties of 4×10^{-4} mM nanocrystal suspension filled in 2 mm fused silica cell and measured using Z-scan technique using 800 nm, 60 fs, 1 kHz pulses at the peak intensity of $\sim$148 GW cm^{-2}. The present study reveals the advantages of Ni incorporation in pure $CsPbBr_3$ nanocrystals on the NLO properties and the advantages of chirped fs DP and ns heating pulses (HP) to generate the tunable XUV radiation in such plasmas for a variety of applications in nonlinear spectroscopy and attosecond physics [40–43].

2. Experimental section/methods

2.1. Materials

The following chemicals are purchased from sigma and TCI as cesium carbonate (Cs_2CO_3, 99.5%), lead bromide ($PbBr_2$, 99.999%), nickel bromide ($NiBr_2$, 99.99%), oleic acid (OA, 90%), and oleylamine (OM, 80%–90%). octadecane (ODE, 99%), toluene (99.8%), and acetone (99.5%), These chemicals are used without further purifications.

2.2. Synthesis of cesium oleate

The precursor for cesium-oleate was created using earlier studies [28]. 1-octadecene (20 ml, ODE), oleic acid, and cesium carbonate were mixed in a 25 ml three-neck round bottom flask (1.25 ml, OA). After heating at 150 °C under N_2 until all of the cesium carbonates had reacted with the OA, the mixed solution was dried at 120 °C under a vacuum for 1 h.

2.3. Synthesis of $CsPbBr_3$ and Ni-doped $CsPbBr_3$ nanocrystals

A 50 ml three-necked round bottom flask was used in the conventional preparation of $CsPbBr_3$ and nickel-doped $CsPbBr_3$ nanocrystals, which involved casting 1 mmol $PbBr_2$, oleylamine (0.5 ml, OM), including oleic acid (0.5 ml, OA). The Ni^{2+} concentration was tuned by varying the concentration of $NiBr_2$ with respect to $PbBr_2$. Further, the mixture was allowed to dry under vacuum for 1 h at 120 °C and heating. After ten minutes, the temperature was increased to 210 °C and held there for another ten minutes to reach this temperature. After that, cesium oleate solution was added to the above reaction mixture with continuous stirring; after five seconds, the reaction mixture was kept in an ice bath for cooling. Then we can separate the nanocrystal plates by centrifuge at 7000 rpm using nonpolar solvents.

During the synthesis process, we optimized the percentage of Ni doping in $CsPbBr_3$ for 0.03%, 0.05%, 0.08%, and 0.1% by choosing the respective weightage 0.066 g, 1 g, 1.74 g, 2.2 g of $NiBr_2$ and 0.367 g of $PbBr_2$ as shown in figure 1(a) in the form of text. However, the basic characterizations include UV-Visisble absorption, photoluminescence (PL), and transmission electron microscopy (TEM) images confirmed the presence of Ni dopants in $CsPbBr_3$ nanocrystals [29]. Briefly, the emission peaks of $CsPbBr_3$ and $Ni_{0.08\%}$ $CsPbBr_3$ were found at 530 and 566 nm, while the absorption peaks were close to 482 nm and 508 nm, respectively. Ni doping did not introduce any new absorption bands, leading to a redshift in the PL spectra.

We calculated the band gap of the materials using absorption spectra in [29]. The corresponding Tauc plots are given in figure 1(b). The obtained band gap for pure $CsPbBr_3$ nanocrystals was 2.281 eV, which decreased to 2.231 eV for $Ni_{0.08\%}$ $CsPbBr_3$ nanocrystals [28]. Further, the pure and doped nanocrystals ($Ni_{0.08\%}$ $CsPbBr_3$) were exposed to TEM analysis (JEM-F200 kV, Gatan Digital Micrograph software) to conform their crystallinity, size, and presence of Ni dopants. The TEM images are shown in figures 1(c)–(f). We observed square-shaped 2D nanoplates with an average particle size of ∼20 nm. The orthorhombic phase of $CsPbBr_3$ was accompanied by the bright lattice fringes reported by high-resolution transmission electron microscopy (HRTEM) with a lattice plane distance of 0.357 nm for pure and 0.350 nm for Ni-doped $CsPbBr_3$ nanocrystals [figures 1(e), (f)]. The obtained Ni-doped and pure $CsPbBr_3$ nanocrystals appeared to have a well-defined crystalline structure depending on the strong and bright diffraction rings in the selected area electron diffraction pattern [insets of figure 1(f)]. The restricted size distribution of nanocrystals in $Ni_{0.08\%}$ $CsPbBr_3$ suggests that doping can impact the homogeneity and size of nanocrystals [28].

2.4. HHG arrangements

From the experimental point of view, there are two immense branches of HHG sources (by conversion from IR-MIR lasers)–gas jets (cells) and LIP harmonics. Gas-jets (cells) sources can provide a more stable source of HHG but require complicated vacuum techniques due to the constant gas feed to a vacuum chamber. Also, traditionally choose of gas is limited to the number of inert gases. In contrast, LIP HHG is not limited by choice of material and does not stress the vacuum system of chambers. At the same time, combined with high repetition rate lasers requires special methods, like rotating targets. Therefore, in the present work, we have used the following experimental scheme for HHG using LIPs of undoped and Ni-doped $CsPbBr_3$ nanocrystals. Figure 2(a) depicts the experimental layout for HHG experiments; the top inset shows existing HHG experimental setup in our laboratory. DP was obtained from Ti: Sapphire laser (Spitfire-Ace, Spectra-Physics), with a central wavelength of 800 nm used for single-color pump (SCP). A 0.2 mm thick beta barium borate crystal (Type I) was inserted in a vacuum chamber on the path of focused 800 nm radiation to implement two-color plasma (TCP) for HHG. The laser was operated at a 100 Hz pulse repetition rate. DP was focused by a 500 mm focal length spherical lens at 0.2 mm above the target and placed in a vacuum chamber. We fixed DP energy at 0.8 mJ (for 35 fs pulses), and the same laser energy was used to convert part of the 800 nm radiation to the second harmonic in the case of TCP. Intensities of chirp-free (35 fs) and chirped pulses (±135 fs) at the focal spot (43.5 μm) were $\sim 4 \times 10^{14}$ W cm^{-2} and $\sim 1 \times 10^{14}$ W cm^{-2}, respectively. The time delay between ns and fs pulses was controlled using a delay generator (Stanford Research Instrument, DG535) triggered by the TTL pulses from the fs laser controller.

Nanosecond pulses (1064 nm, 7 mJ, 5 ns, 10 Hz, Nd: YAG, Q-smart, Coherent, USA) were focused on the target surface using a 200 mm spherical lens and produced the plasma containing nanocrystals. The focal spot of ns pulses was 34.5 μm, and its intensity on the target surface was $\sim 4 \times 10^{10}$ W cm^{-2}. The XUV spectrometer, consisting of a cylindrical mirror, flat-field grating, and microchannel plate (MCP), analyzed the emitted harmonics. A charge-coupled device (CCD) camera registers the emitted harmonics by viewing the phosphorous screen of the MCP. To capture the harmonics spectra, we have fixed the CCD camera settings gain 100, and Red, Green, and Blue pixels are adjusted to (0, 100, 0) for the whole set of measurements. To analyze the intensity of harmonics for each harmonic spectra, we developed a program in MATLAB, which covers the selected region of harmonic spectra in pixels and further used summation along the *X*-axis for the pixels and obtained line profiles. Our measurements can be considered relative to the 9th-order harmonic (9H), which is first detectable by our MCP detector. Common estimations for conversion efficiency are in the range 10^{-5}–10^{-7} for the HHG plateau in the case of gas-jet harmonics sources [1–3]. The approach we used might be enough to correlate the tendency of harmonics intensity (in arbitrary units) emitted from nanocrystals.

To achieve positively/negatively (±) chirped pulses, the distance inside the optical compressor of the laser was adjusted by moving horizontal retroreflector towards right or left sides regarding chirp-free conditions [figure 2(a)]. In that

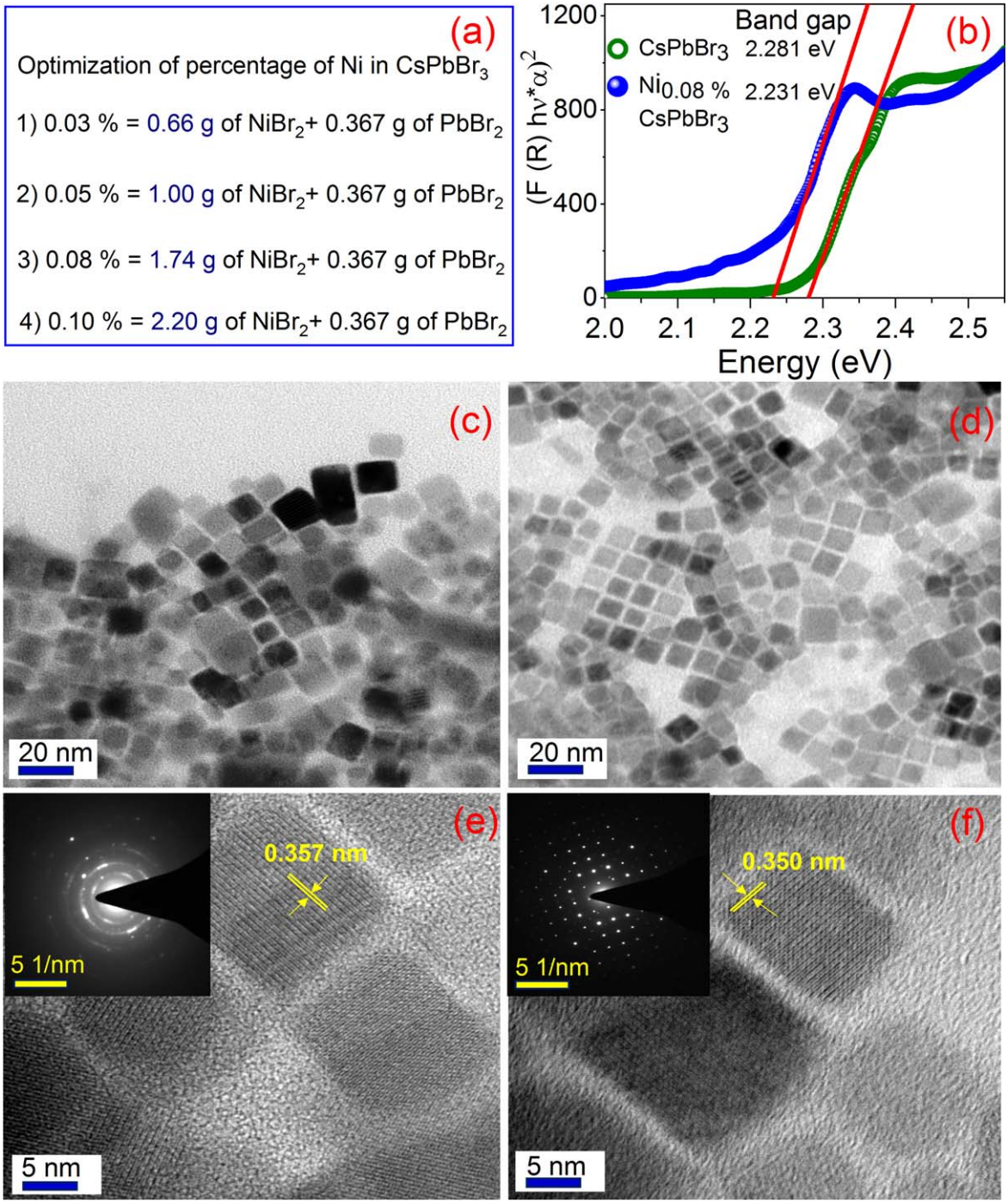

Figure 1. (a) Optimization of Ni % in $CsPbBr_3$ (b) Tauc plot for pure $CsPbBr_3$ and Ni $_{0.08\%}$ $CsPbBr_3$ (c), (d) low magnification images of pristine and Ni-doped $CsPbBr_3$ (e), (f) HRTEM image of pristine and Ni-doped $CsPbBr_3$ (SAED patterns are shown in the insets).

case, pulse duration varied from 35 to 135 fs. In the case of negatively chirped pulses, blue and red components of the laser spectrum were re-distributed towards the leading and trailing parts of DP, respectively. In the case of positively chirped pulses, the red/blue component occupied the leading/tailing front of the pulse. Figure 2(b) shows the spectro-temporal distributions of chirp-free 35 fs and chirped 135 fs pulses. Spectral profiles of chirped and chirp-free pulses for SCP and TCP are shown in figures 2(c) and (d), respectively. The details of perovskite nanocrystal preparation for HHG are presented elsewhere [26, 27]. Briefly, nanocrystals were dissolved in toluene and deposited on a glass substrate. The thickness of the deposited film was 1 mm. The film containing these nanocrystals had an approximate length of 8 mm and a width of 6 mm. The glass substrates with deposited nanocrystals were placed in the target chamber (figure 2(a)) and further ablated by ns HP. Pure $CsPbBr_3$ and four samples containing different concentrations of Ni were kept one after another on the glass slide and moved using the XYZ stage during the laser ablation of nanocrystals.

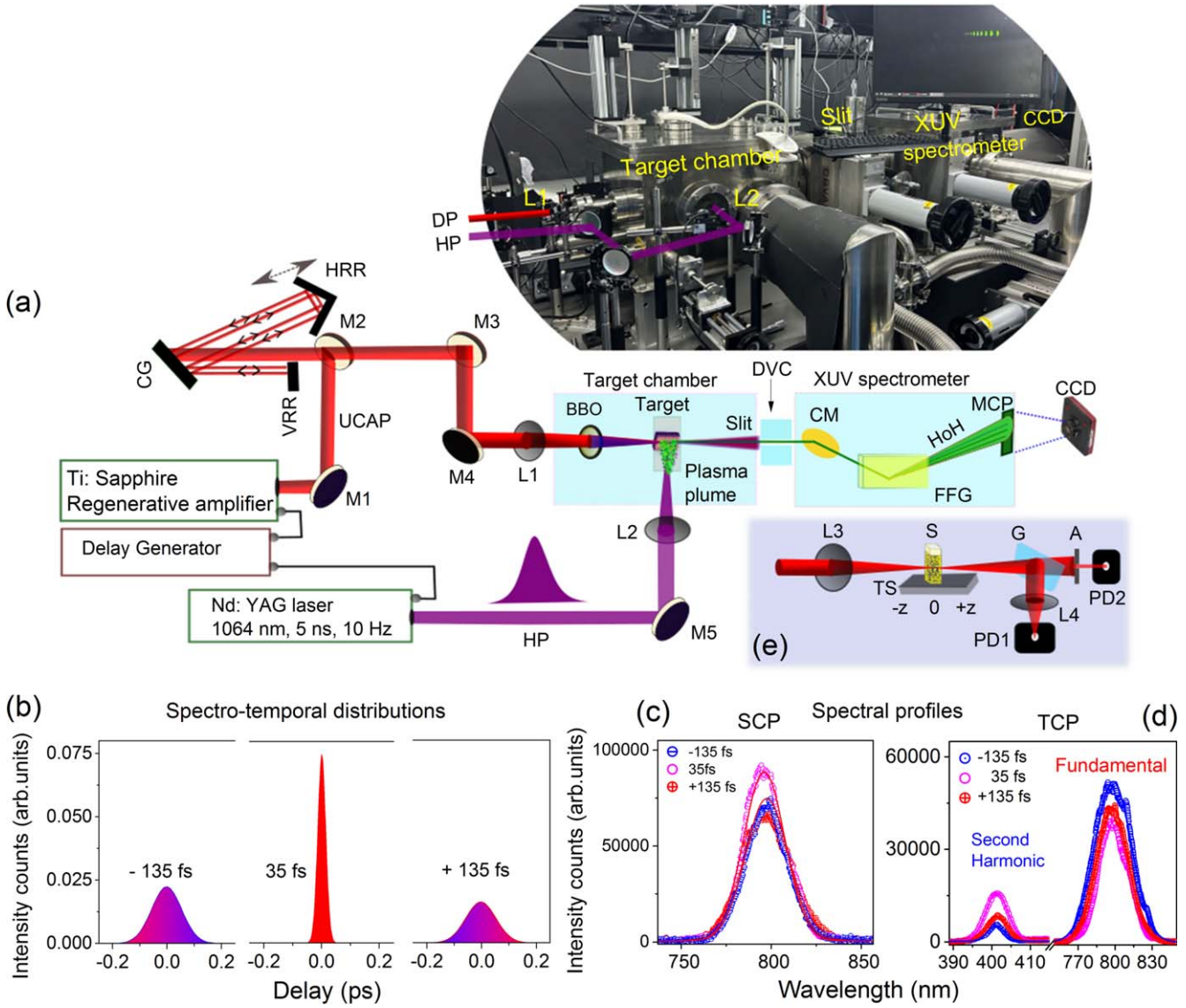

Figure 2. (a) Experimental layout for HHG (top: image shows the existing HHG setup in our laboratory). The uncompressed amplified laser pulse (UCAP) was directed by a mirror (M1) to the compressor comprising the compressing grating (CG), vertical retroreflector (VRR), and horizontal retroreflector (HRR). Compressed driving pulse (DP) was focused by a spherical lens (L1, f = 500 mm) inside the plasma. In the case of TCP, beta barium borate (BBO) was inserted on the path of focused radiation and produced laser plasma on the surface of the target. Generated high-order harmonics (HoH) and fundamental radiation propagated through slit and differential vacuum chamber (DVC). They entered the XUV spectrometer comprising the cylindrical mirror (CM), flat-field grating (FFG), and microchannel plate (MCP). A CCD camera registered the harmonic spectrum. (b) Spectro-temporal distributions of chirp-free and chirped pulses. (c, d) Spectral profiles of (c) single color pump (SCP) and (d) two color pump (TCP) of chirp-free 35 fs pulses and positively and negatively chirped 135 fs pulses. (e) Z-scan setup: L3 and L4: lenses (f = 400 mm, and 100 mm); S: sample (2 mm thick quartz cuvette filled with nanocrystal suspension); G: glass; A: aperture; PD1 and PD2: photodiodes for the measurements of propagated radiation in the case of open-aperture and closed-aperture schemes, respectively.

2.5. Z-scan setup

Figure 2(e) shows the experimental layout for the Z-scan measurements. We used 800 nm, 60 fs pulses as the probe radiation having a pulse energy of 22 nJ. A 400 mm lens focused the laser pulses. The measured 1 e^{-2} focal spot of the input laser pulse was 38.5 μm, and the corresponding peak intensity (I_0) equals 148 GW cm^{-2}. We used 4 $\times$ 10^{-4} mM nanocrystal solution (in toluene) filled in a 2 mm fused silica cuvette, which was moved along the *Z*-axis by the motorized translation stage. The transmitted laser pulse from the sample was registered by photodiodes 1 and 2, and the photodiode signal was fed to the lock-in amplifier (SR830, Stanford Research System) for measurements of open-aperture (OA) and closed-aperture (CA) schemes at each position of the sample. LabView software controlled the lock-in amplifier, and the translation stage was monitored through a personal computer.

2.6. Theoretical equations for Z-scan measurements

It is well recognized that Z-scan is a potential technique to measure materials' third-order NLO properties. The values of third-order nonlinear absorption coefficient (β), saturation

intensity (I_{sat}) and nonlinear refraction index (γ) can be measured using the analysis of the Z-scan technique through OA and CA measurements, respectively. In the case of Z-scan measurements, the two-photon absorption (TPA), saturable absorption (SA), the combined process of SA+reverse saturable absorption (RSA), nonlinear refraction and absorption (NRA), and NRA + SA induced normalized transmittance of laser pulses can be described through the equations (1) to (5) [44, 45]

$$T_{\mathrm{TPA}}(z) \approx 1 - \frac{q}{2\sqrt{2}} \tag{1}$$

$$T_{\mathrm{SA}}(z) = 1 + \frac{I_0}{I_{\mathrm{sat}}(x^2+1)} \tag{2}$$

$$T_{\mathrm{SA+RSA}}(z) = \left(1 - \frac{q}{2\sqrt{2}}\right) \times \frac{I_0}{I_{\mathrm{sat}}(x^2+1)} \tag{3}$$

$$T_{\mathrm{NRA}}(z) = 1 + \frac{2(-\rho x^2 + 2x - 3\rho)\Delta\Phi_0}{(x^2+1)(x^2+9)} \tag{4}$$

$$T_{\mathrm{NRA+SA}}(z) = 1 + \frac{2(-\rho x^2 + 2x - 3\rho)\Delta\Phi_0}{(x^2+1)(x^2+9)} + \frac{I_0}{I_{\mathrm{sat}(x^2+1)}}. \tag{5}$$

Here, $q(z) = I_0 \times \beta \times L_{eff} /(1 + z^2/(z_0)^2)$, I_0 is the peak intensity of excitation laser pulse, $x = z/z_0$, $z_0 = kw_0^2$ is the Rayleigh length, $k = 2\pi/\lambda$ is the wavenumber, w_o is the radius of the beam waist, and $\Delta\Phi_0 = k\gamma I_0 L_{\mathrm{eff}}$ is the phase change due to nonlinear refraction ($\gamma = \Delta\Phi_0/kL_{eff}I_0$), $L_{eff} = [1 - \exp(-\alpha_0 L)]/\alpha_0$ is the effective length of the nonlinear medium, α_0 is linear absorption coefficient, L is sample thickness. The above equations (1) to (5) are considered for the laser beam should possess a Gaussian profile (Spatial profiles of laser pulses shown in figure 2(c) are close to Gaussian beams).

3. Results and discussion

3.1. HHG from nanocrystal plasma plumes

The harmonics spectra generated from the LIPs of nanocrystals could be influenced by several important parameters such as DP wavelength (SCP, TCP), peak intensity, chirp, as well as HP duration and its intensity. Also, the delay between the DP and HP plays a pivotal role in the emission of harmonics from LIPs. In our earlier work [30], we covered the DP intensities between 1.2 to 6.0 $\times$ 10 ^{14} W cm^{-2} in the case of ps LIPs. It is observed that the increase in the intensity of harmonics and cut-off with respect to the DP intensity increase. In the present case, we have chosen the optical DP intensity i.e. 4 $\times$ 10 ^{14} W cm^{-2} for chirp-free laser pulses and 1 $\times$ 10 ^{14} W cm^{-2} for chirped pulses, and the HP intensity 4 $\times$ 10^{10} W cm^{-2}.

Meanwhile, the pulse duration of fundamental and second harmonics also influences the harmonic spectra in the case of TCP. We have theoretically determined the pulse duration for the second harmonic wavelength at ω = 800 nm, $I_{35\mathrm{fs}} = 4 \times 10^{14}$ W cm^{-2}, $I_{135\mathrm{fs}} = 1 \times 10^{14}$ W cm^{-2}. The corresponding second harmonic wavelength duration was obtained at 47 fs and 100 fs [46]. The intensity of 400 nm is equal to $I_{2\omega} \sim 2.1 \times 10^{13}$ W cm^{-2}. For these reported nanocrystals, in the case of SCP using chirp-free 35 fs pulses, the maximum harmonic signal was achieved in the delay range of 200–400 ns. The corresponding first maxima were identified at 400 ns delay for $CsPbBr_3$, 300 ns delay for $Ni_{0.03\%}$ and $Ni_{0.05\%}$, and 200 ns delay for $Ni_{0.08\%}$ and $Ni_{0.10\%}$.

Figures 3(a) and (b) show the raw images of harmonic spectra obtained from five nanocrystals in the case of SCP and TCP for chirp-free 35 fs and chirped 135 fs pulses. The upper, middle and bottom spectra in each panel correspond to the DP of +135 fs, 35 fs and −135 fs durations, respectively. Harmonic spectra contain only odd harmonics for SCP and both odd and even harmonics in the case of TCP while demonstrating stronger harmonics. A denser electron wave packet and a higher ionization rate for TCP lead to the selection of a short quantum path component. As a result, the harmonic yield was stronger for TCP compared to SCP [47–49]. In the case of $CsPbBr_3$, the harmonics shift is clearly visible in the upper panels of figures 3(a) and (b). The positively and negatively chirped DP depict the impact on spectral shift, harmonic cut-off, and intensity distribution. In previous studies, the corresponding spectral shift was explained by the role of the leading part of pulse [31, 50, 51]. The harmonics are commonly generated by the leading part of the laser pulses. Correspondingly, the abundance of either blue or red component of a chirped pulse will shift the harmonic wavelength towards the blue or red side with regard to the harmonics generated by chirp-free pulses [46]. Thus the negative chirp leads to a shift of harmonics toward the shorter-wavelength side (blue shift), and the positive chirp of DP leads to a shift of harmonics toward the longer-wavelength side (redshift).

Different percentages of Ni-doped in $CsPbBr_3$ nanocrystals demonstrated a different shift of harmonic spectra. In figure 3, we show the raw images of the obtained harmonic spectra. Presentation of experimental data as images appearing on the computer screen rather than groups of intensity distributions is aimed at better viewing obtained data and demonstrating the difference between HHG in the case of chirp-free and chirped pulses. We want to stress that the goal of these studies was a qualitative definition of the influence of Ni concentration on the harmonic spectra and conversion efficiency in two cases (SCP and TCP) rather than the quantitative measurements of gain of harmonics in the plasmas. We also would like to underline that raw images were taken at saturation conditions of CCD camera for better viewing of peculiarities of harmonic distribution. The harmonic spectra [figure 3(b)] demonstrate that all nanocrystals show harmonics saturation in the case of chirp-free 35 fs TCP. $Ni_{0.05\%}$ $CsPbBr_3$ shows harmonics saturation for SCP using chirp-free and chirped DP. Notice that all lineouts presented below were obtained at the unsaturated conditions of registration for analysis of harmonics intensity and shift of harmonics.

Figure 4 depicts the lineouts of harmonic spectra for SCP and TCP, respectively. Harmonic intensities and their

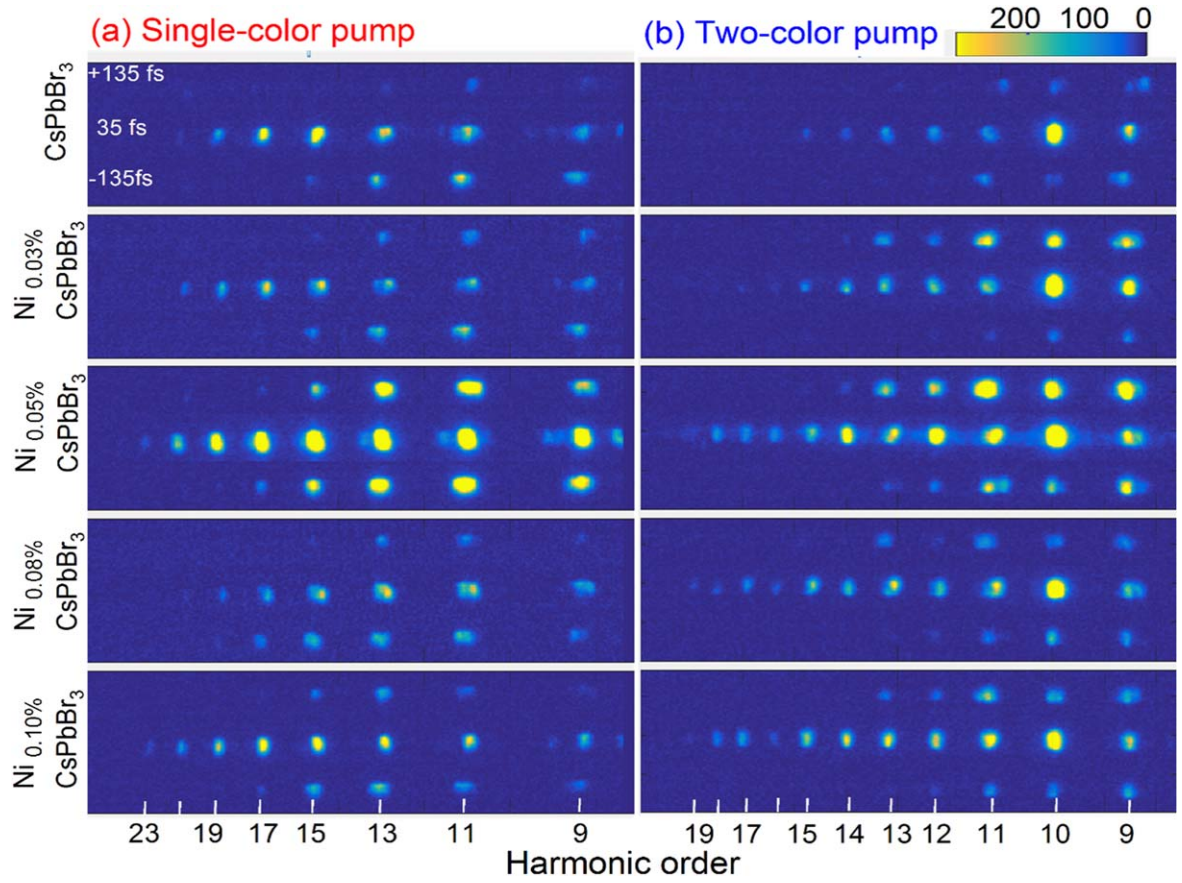

Figure 3. The raw images of harmonic spectra were obtained from nanocrystals in the case of (a) single-color and (b) two-color pumps for chirp-free 35 fs and chirped 135 fs pulses. Each panel's upper, middle, and bottom spectra correspond to the driving pulses of +135 fs, 35 fs, and −135 fs durations, respectively. Experiments were carried out using the targets containing different concentrations of Ni in perovskite nanocrystals.

positions are varied for different ablated nanocrystals due to variations in the plasma components. In the case of SCP chirp-free 35 fs pulses, harmonics from pure $CsPbBr_3$ possess a maximum intensity at around the fifteenth harmonic (15H), which is changed to 17H for Ni $_{0.03\%}$ and Ni $_{0.10\%}$ and 13H for $Ni_{0.08\%}$ -$CsPbBr_3$ nanocrystals. Whereas Ni $_{0.05\%}$ $CsPbBr_3$ shows a plateau pattern up to 19H. However, in the case of TCP, all nanocrystals show maximum intensity at 10H. Due to the strong influence of the shorter-wavelength pump (400 nm), even harmonics' intensity is higher than that of the odd harmonics.

Meanwhile, in the case of chirped DP, it is interesting to note that the distribution of harmonics intensity might increase/decrease in the lower orders harmonics (i.e. 9H, 11H, 13H in case of SCP, 9H, 10H, 11H, 12H, 13H for TCP) region. This increment or decrement in the intensity of harmonics for lower orders depends on the plasma density. Suppose we could achieve a higher intensity of 9H. In that case, 10H in the case of chirped DP compared to the chirp-free free pulses. In that case, one can assume that the supplied chirped DP intensity could emit initial harmonics with higher intensity due to the reduced peak intensity. In contrast, the chirp-free pulses lead to enhance the other higher orders. For example, as shown in figure 4(a), in the case of -135 fs pulses, $CsPbBr_3$ shows highly intense harmonics at 9H, 11H, and 13H, whereas for 35 fs pulses leads to enhancement in 15H and 17H than the lower orders. For other conditions, the shorter 35 fs chirp-free pulses possess higher harmonics intensity than chirped pulses.

Figures 5(a) and (b) illustrate the normalized HHG spectra between 9H and 15H in the case of SCP and TCP, respectively, which represent examples of harmonic shifts. We also present the measured harmonic shifts in figures 5(c) and (d) in the case of positively and negatively chirped pulses with regard to the chirp-free pulses for the harmonics 9H, 11H, 13H (SCP), and 9H, 10H, 11H, 12H (TCP). We chose a few harmonics in the case of chirped pulses to compare the shift for 35 fs pulses due to the limitation of harmonic cut-off achieved by less intense chirped pulses. The peak intensity of chirped pulses was almost four times less than that of chirp-free pulses due to increased pulse duration. As per the energy cut-off formulae $E_{\mathrm{cut-off}} = I_p + 3.17U_p$. Where I_p is the ionization potential, $U_p = 9.33 \times 10^{-14} I\,(W\,\mathrm{cm}^{-2})\,\lambda^2\,(\mu m)$ [52]; the cut-off harmonics is directly proportional to the intensity (I) and wavelength (λ) of fs DP. Therefore, the chirped laser pulses (higher pulse duration) decrease their peak intensity. In contrast, at fixed laser energy, the much shorter duration of fs DP leads to an increase in the harmonic cut-off. The shorter wavelength of 400 nm currently leads to a

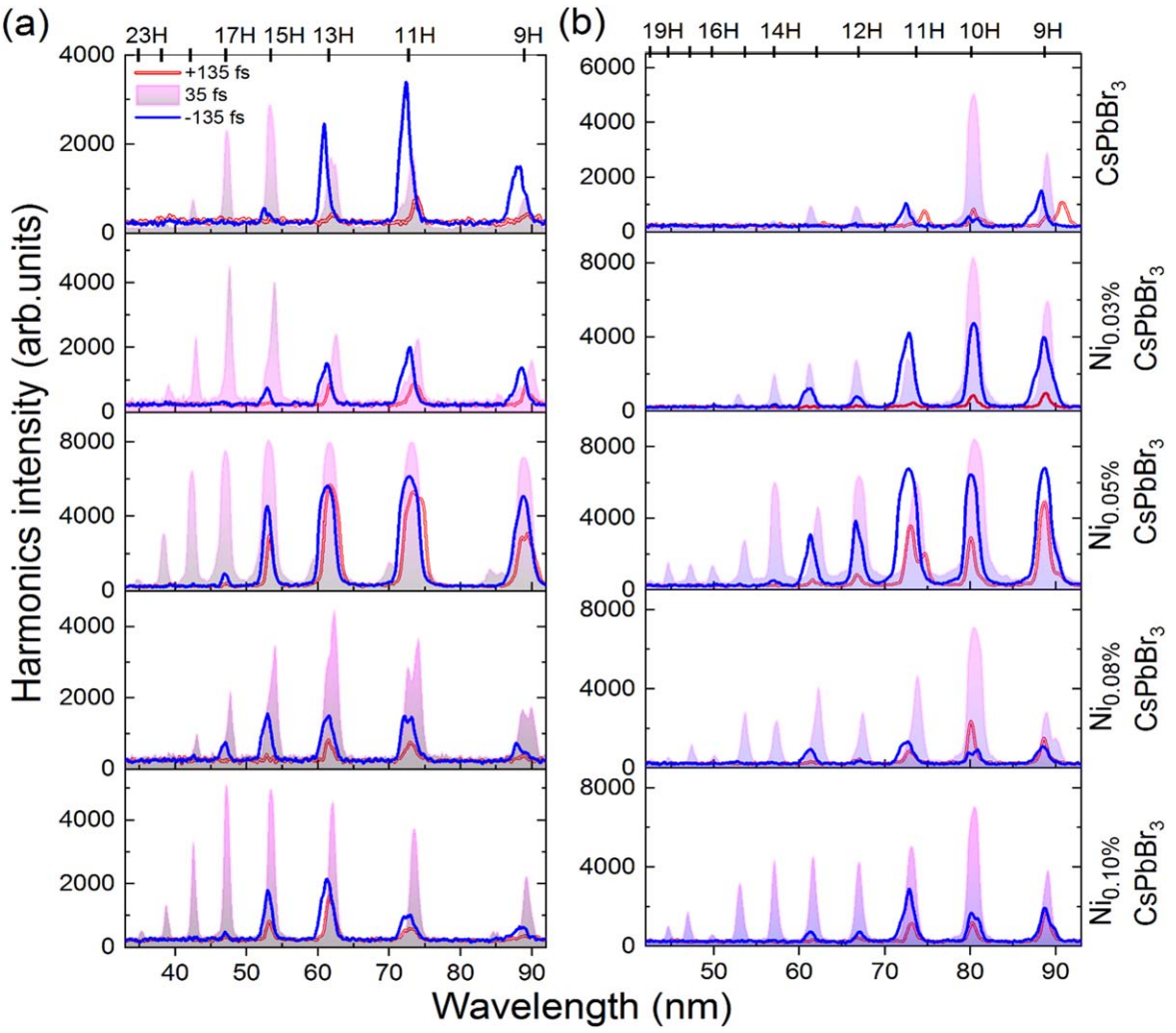

Figure 4. The lineouts of harmonic spectra for $CsPbBr_3$ and Ni-doped $CsPbBr_3$ nanocrystals (top to bottom panels) in the case of (a) single-color and (b) two-color pumps using the chirp-free 35 fs and chirped 135 fs pulses.

decrease in the cut-off of studied nanocrystals, which is limited to 19H for TCP and extended to 23H for SCP.

Figures 5(c) and (d) show the measured spectral shift for chirped pulses. In the case of SCP, the blue shift of 9H is decreased for Ni-doped nanocrystals compared with pure $CsPbBr_3$, whereas the reverse phenomenon was observed in the case of TCP. In both cases (SCP and TCP), most harmonics possessed higher redshift for Ni-doped $CsPbBr_3$ nanocrystals than pure $CsPbBr_3$ (except for 11H in TCP). At the same time, the blue shift of harmonics decreased in both DP (except 9H for TCP). Based on the data shown in figure 5(c) in the case of SCP [applicable to TCP, figure 5(d)], the red shift in the harmonics is more prominent in the case of Ni-doped nanocrystals, which indicates that the Ni-components are might frequently interact with longer wavelengths of the chirped DP. Consequently, the blue shift is higher for $CsPbBr_3$ than Ni-doped $CsPbBr_3$ nanocrystals. It is inferred that there might be convolution between Ni dopants (interacts with a higher edge of blue components) and $CsPbBr_3$ (interacts with a lower edge of blue components) plasma components which lead to a decrease in the blueshift for Ni-$CsPbBr_3$.

A similar opposite behavior was observed in the case of Z-scan data. $CsPbBr_3$ possessed strong TPA or RSA at a focal position and Ni- leads to shows SA. The overall results decrease the TPA/RSA process, and the results are described in the next section, 3.2. Therefore, it is assumed that Ni-dopants play a crucial role in the spectral distribution of emitted harmonics in the case of chirped DP. Anyway, one has to evaluate the presence of plasma components and their density quantitatively to examine the proper mechanism for this variation in the spectra shift with respect to percentage changes in the Ni doping to $CsPbBr_3$ nanocrystals.

3.2. Third-order NLO properties measured using the Z-scan technique

Earlier, Ketavath *et al* demonstrated the NLO properties of 2D nanocrystals (1 mm suspension) using 800 nm, 70 fs, and 1 kHz pulses at a peak intensity of 90 GW cm^{-2} [29]. However, in the present case, we increased the volume of nanocrystal suspensions (4×10^{-4} mM concentration nanocrystal suspension filled in a 2 mm fused silica cell). We used a slightly higher peak intensity of input laser pulses

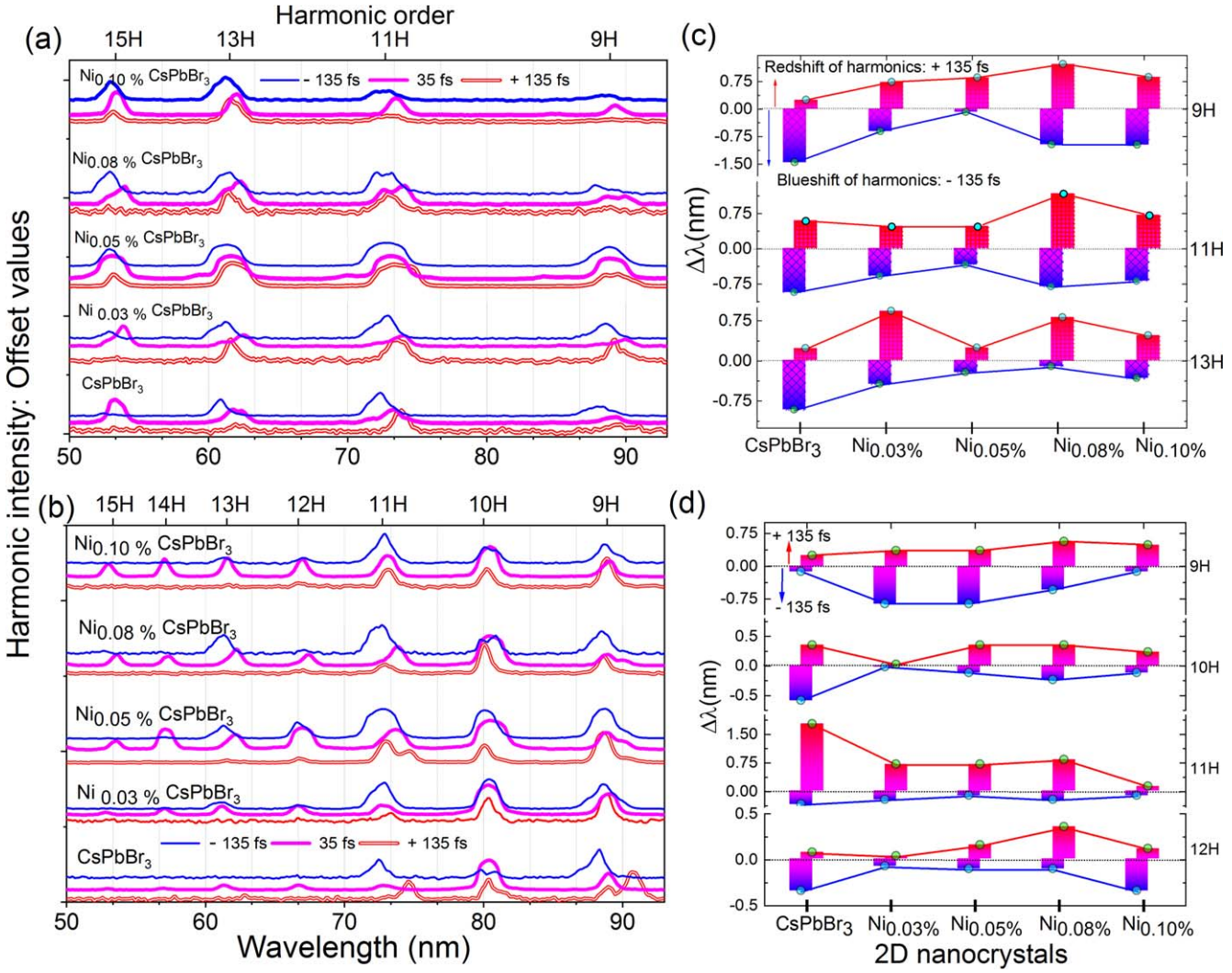

Figure 5. Normalized HHG spectra between 9H and 15H in the case of (a) single-color pump and (b) two-color pump, representing the patternsof harmonic shifts. Here we also present the measured harmonic shifts in the case of positively and negatively chirped pulses for the chirp-free pulses for the harmonics (c) 9H, 11H, 13H in the case of SCP, and (d) 9H, 10H, 11H, 12H in the case of TCP.

(148 GW cm^{-2}). In the present case, nonlinear absorption and refraction processes were changed due to increased Ni weight percentages. Figures 6(a) and (b) depict the OA and CA Z-scan curves for five 2D nanocrystals. It was observed that there are no changes in the nonlinear absorption process (TPA) for pure $CsPbBr_3$ and Ni $_{0.03\%}$-$CsPbBr_3$ compared to earlier work [29]. Whereas a further increase in Ni percentages, i.e. from 0.05% to 0.10%, the TPA switches to SA + RSA.

In figure 6(a), one can see that the dip value at the focus position is moved upward and increases the SA process. The obtained nonlinear absorption coefficient for pure $CsPbBr_3$ equals 1.69×10^{-11} cm W^{-1}. The value is decreased to 1.27×10^{-11} cm W^{-1} for $Ni_{0.03\%}$ $CsPbBr_3$ due to the contribution of 0.03% Ni, which possesses SA at the focal spot (dip value is increased compared to $CsPbBr_3$, half-up circles shown in figure 6(a) compared to open circles), and measured I_{sat} for 0.03% Ni is 3.02×10^{11} W cm^{-2}. However, $Ni_{0.05\%}$, $Ni_{0.08\%}$, $Ni_{0.10\%}$ -doped $CsPbBr_3$ nanocrystals possess SA (corresponding I_{sat} values are 2.01×10^{11}, 1.56×10^{11} and 1.18×10^{11} W cm^{-2}) away from the focal region. The vital RSA process predominates in the focal region, which leads to an increase in the nonlinear absorption coefficient, which is given by 2.55×10^{-11}, 2.93×10^{-11} and 3.03×10^{-11} cm W^{-1}, respectively. Similarly, in the case of CA Z-scan measurements, it was achieved that $CsPbBr_3$ possess a clear NRA (self-focusing) process (open circles shown in figure 6(b), and the theoretical fit is symmetrical). Ni-doped $CsPbBr_3$ leads to an increase in the saturation process, which leads to an increase in the transmittance (the curves are unsymmetrical with increased peaks). Therefore, it is inferred that an increase in the volume of Ni-$CsPbBr_3$ nanocrystals leads to a growth in the saturation process. The obtained data were fitted with equation (5), i.e. the combination of NRA + SA. The measured γ values for $CsPbBr_3$ and ($Ni_{0.03\%}$, $Ni_{0.05\%}$, $Ni_{0.08\%}$, $Ni_{0.10\%}$)-doped $CsPbBr_3$ nanocrystals are given by 9.03, 9.58, 9.13, 9.35, and 9.86×10^{-16} cm^2 W^{-1}, respectively. Meanwhile, the CA curves shown in figure 6(b) look like in the case of the earlier work [29]. In that case, they considered only NRA; therefore,

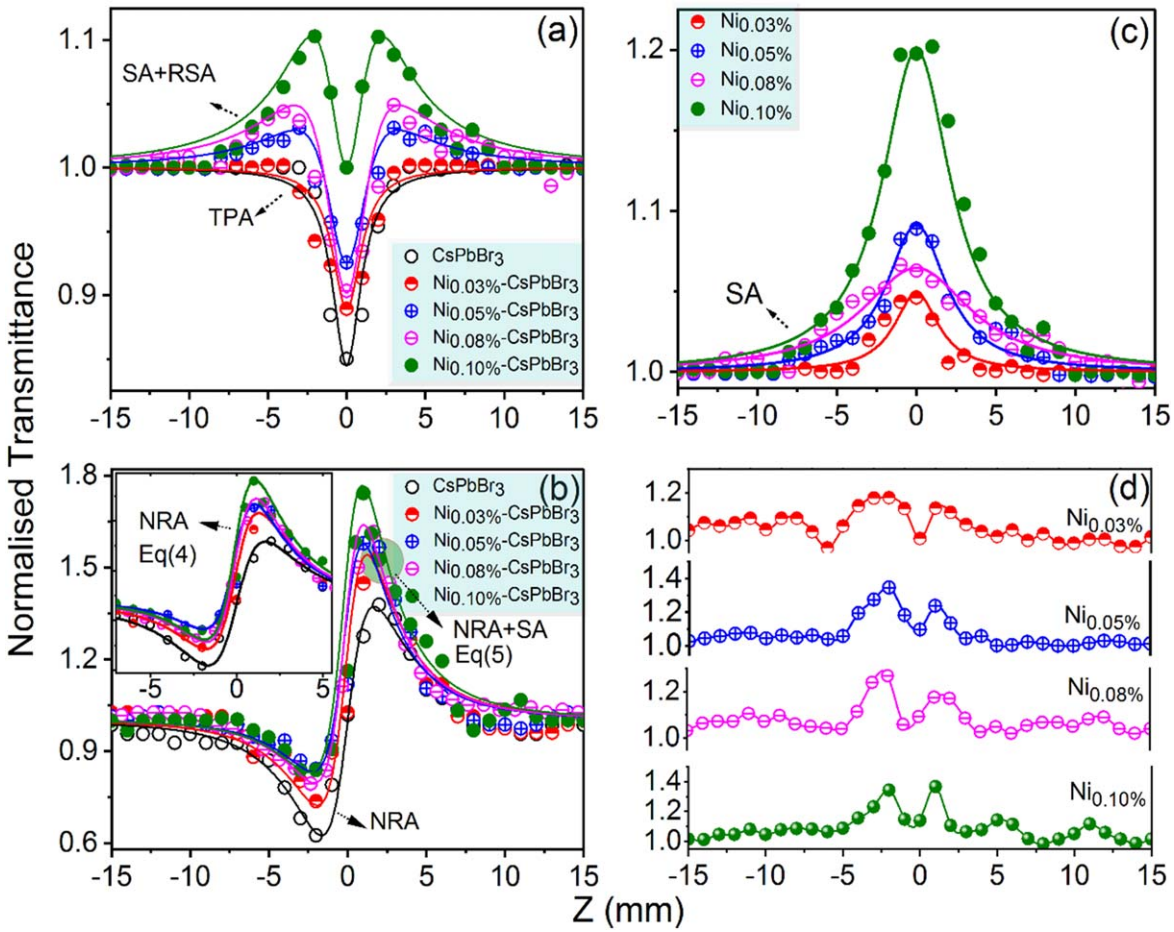

Figure 6. Z-scan curves for five 2D nanocrystals (a) open-aperture (OA), (b) closed-aperture (CA) measurements. Inset shows data fitted with equation (4), considering only NRA for all nanocrystals. The ratio curves (Ni-$CsPbBr_3$ to pure $CsPbBr_3$) were obtained in the case of (c) OA and (d) CA data. In (a)–(c) open symbols represent the experimental data while the solid lines are theoretical fits.

we fitted again these CA data using equation (4) for Ni-doped $CsPbBr_3$ nanocrystals, as shown in the inset of figure 6(b). Equation (4) was fitted nicely with presented CA data with excluded saturation process. In this case γ values obtained for $Ni_{0.03\%}$, $Ni_{0.05\%}$, $Ni_{0.08\%}$, $Ni_{0.10\%}$ -doped $CsPbBr_3$ nanocrystals are 10.68×10^{-16},10.41×10^{-16}, 11.07×10^{-16}, 12.14×10^{-16} $cm^2\,W^{-1}$, respectively. In both cases, the trend of the achieved γ values are similar for Ni-$CsPbBr_3$ nanocrystals (figure 7(c), bottom panel).

The nonlinear refractive indices seem to be lower in the current work ($I_0 = 148$ GW cm^{-2}) compared to the earlier work ($I_0 = 90$ GW cm^{-2}) [29]. Ideally, the excitation fluence should not impact the nonlinear coefficients. It is valid for the small fluence of the excitation pulses. It is well recognized in the literature that raising input intensity leads to excitation from higher energy levels. SA process can change to the RSA process and vice versa depending on the input peak intensities [53, 54]. The presence of additional/higher-order NLO processes modifies the NLO coefficients when there are excitations into the higher energy state. We saw that Ni-dopants' presence significantly impacted the nonlinear absorption and refraction processes. By dividing the contribution of pure $CsPbBr_3$ from the Z-scans of Ni-doped $CsPbBr_3$ nanocrystals, it was determined that Ni-counterparts had SA at the focus. The relevant division data for OA and CA Z-scans are displayed in figures 6(c) and (d). The graphs further demonstrate that the SA peaks exhibit a nonlinear expansion when the percentile change of Ni-dopants increases. Although, there is a small dip in focus in the case of CA due to the phase changes.

3.3. Correlation between HHG yield/cut-off and third-order NLO properties

The maximum harmonic intensity and cut-off obtained from data shown in figure 4 are presented in figures 7(a) and (b) for chirp-free 35 fs pulses and chirped ±135 fs pulses. The curves for chirped pulses are almost identical in shape to chirp-free 35 fs pulses and reveal the contribution of Ni to the change of emission of high-order harmonics. Our previous studies reported that improvement of harmonic intensity for chirp-free 35 fs (plasma produced by ps and ns pulses) was nearly proportional to the third-order NLO parameters of nanocrystals at 800 nm and saturation intensities at 400 nm [29–31]. Likewise, this relationship is almost similar for chirped DP (135 fs) in the case of ps LIP reported in [31].

Consequently, in the present case, harmonic intensity and cut-off enhancement pattern also match current and earlier

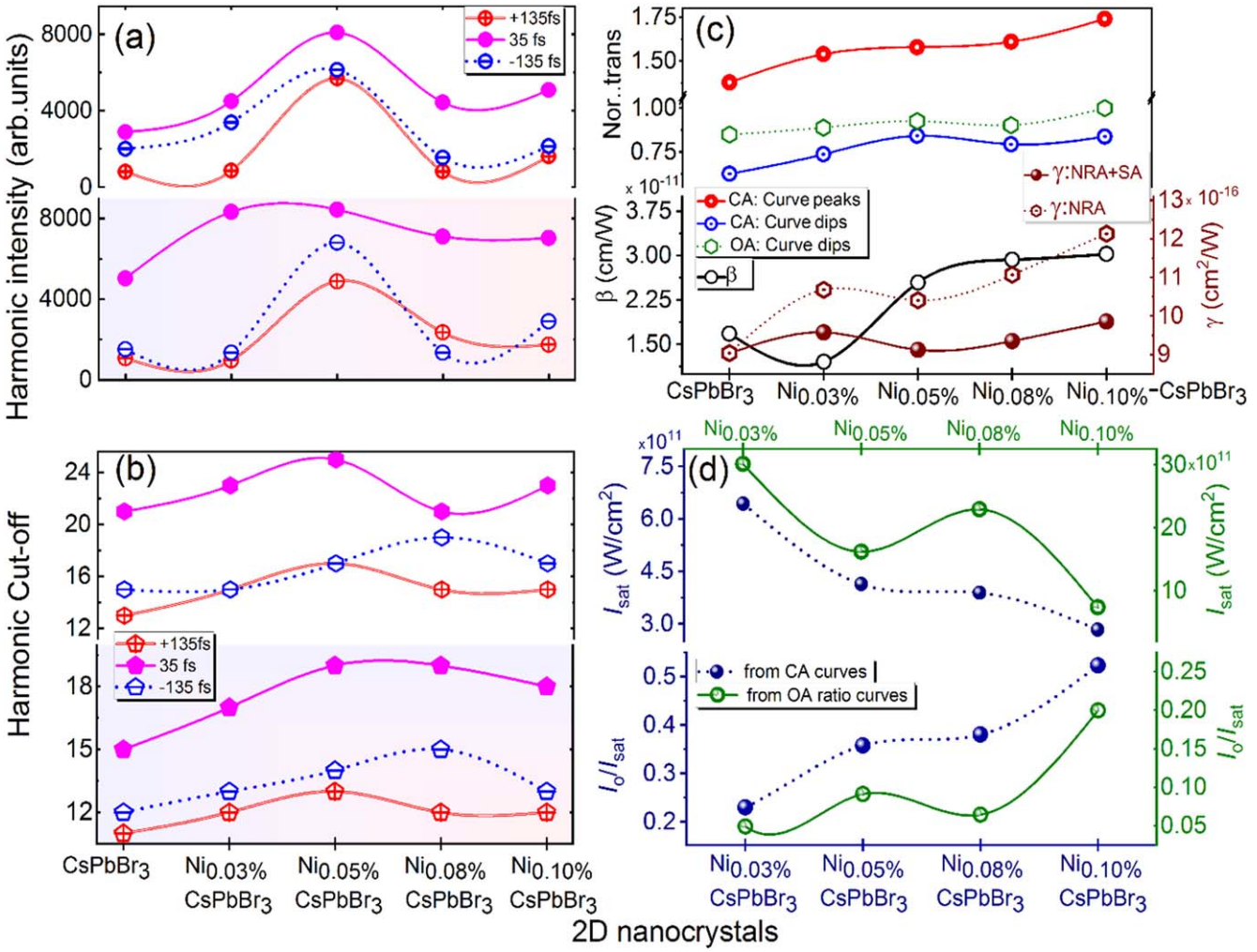

Figure 7. Evaluation of (a) the maximum harmonic intensity and (b) cut-off in the case of the single-color pump (upper panel) and two-color pump (bottom panel) obtained in the Ni-doped nanocrystals, respectively. (c) peak and dip positions of transmittance for closed and open aperture curves (upper panel), nonlinear absorption and refraction coefficients (bottom panel), (d) saturation intensities and the ratio of saturation intensities for Ni-doped $CsPbBr_3$ (left *Y*-axis, upper and bottom panels), and Ni-$CsPbBr_3$/$CsPbBr_3$ (Top *X*-axis, right *Y*-axis; upper and bottom panels) respectively.

measurements for ns LIP and chirped DP. Figure 7(c) shows the trend of peak and dip positions of normalized transmittance for OA and CA measurements [figure 7(c), upper panel] and obtained β and γ values (in the case of NRA and NRA + SA, figure 7(c), bottom panel) for pure and Ni-doped $CsPbBr_3$ nanocrystals. The obtained NLO parameters are higher for Ni-doped $CsPbBr_3$ than pure $CsPbBr_3$. Figure 7(d) depicts the saturation intensities (I_{sat}) and the ratio of I_0/I_{sat} for four Ni-doped $CsPbBr_3$ (left *Y*-axis, upper and bottom panels) and Ni-$CsPbBr_3$/$CsPbBr_3$ (right *Y*-axis; upper and bottom panels), respectively. Ni-doped samples showed lower I_{sat} values relative to their % changes before and after the deduction of pure $CsPbBr_3$ contribution from Ni-$CsPbBr_3$ nanocrystals. The nanocrystals, in this instance, conveyed more energy than the pure nanocrystals. The current study again confirms that the third-order NLO coefficients for Ni-doped $CsPbBr_3$ are higher than the pure $CsPbBr_3$.

The improved NLO properties might be due to the localized surface plasmon-induced charge transfer. Meanwhile, in the present report, we have measured the higher-order harmonics from LIPs of reported un-doped and Ni-doped $CsPbBr_3$ nanocrystals. It is familiar that HHG is a three-step model [55] [(i) ionization by the strong laser field, (ii) acceleration in the laser field, and (iii) recombination with the parent ion and emission of a high energy photon] and emission of harmonics extensively depend on the plasma components of parent nanocrystals (atoms, ions and nanoparticles). The produced harmonics spectra result from individual harmonics released by each element in the plasma plumes. The cut-off and intensity of harmonics could increase with respect to an increase in the ionization potential (I_p) of plasma components. The first ionization potential of Cs is 3.89 eV, Pb is 7.42 eV, Br is 77.81 eV, and Ni-7.64 eV, and the second ionization potentials for Cs, Pb, Br, and Ni are given by 23.16, 15.03, 21.8, and 18.17 eV, respectively. The provided chirp-free DP intensity is enough to iterate the harmonics from either atoms or ions or both. Therefore, due to the decrease in the peak intensity of chirped pulses, only the atoms and the singly charged ions of plasma components could be expected to generate the harmonic spectra.

Meanwhile, the Ni-doped nanocrystals contain more Ni atoms or ions in the plasma components than the un-doped $CsPbBr_3$ nanocrystals. There is a change in Ni-percentage from one to another nanocrystals (i.e. 0.03% to 0.1%). Therefore, the plasma density of Ni-doped nanocrystals is expected to be higher than the un-doped $CsPbBr_3$ nanocrystals; as a result, high intense harmonic is emitted, which results in to increase in the harmonic shift in case of chirped DP. Experimentally, we cannot directly distinguish or quantify the contributions of plasma components. It is because the plasma always contains ions of different charge states, and we could not freely manipulate their relative concentrations. Nevertheless, as discussed above, we could estimate their contributions by assuming the total HHG yield is proportional to the plasma (ion) density. Overall, the tendency of HHG curves for harmonic intensity, the cut-off for chirped and chirp-free pulses, and the redshift/blueshift (data points figures 5(c) and (d)) of harmonics look similar to third-order NLO properties.

4. Conclusions

We analyzed the high-order harmonic generation in the case of SCP and TCP chirp-free and chirped DP from LIPs of undoped and Ni-doped $CsPbBr_3$ nanocrystals. The LIPs produced by nanocrystal surface ablated with nanosecond HP. Also, it has been shown that in the case of $NiCsPbBr_3$ nanocrystals, the presence of Ni-dopants improves third-order NLO properties. Similarly, the plasma components of Ni and $CsPbBr_3$ plasma lead to an improvement in the harmonics emission. In the case of chirped DP, it was observed that the spectral shift was also enhanced in the case of Ni-doped nanocrystals. Thus, these nanocrystals can be used to establish tunable XUV sources. The NLO parameters determined by the Z-scan technique utilizing an excitation wavelength of 800 nm and HHG yields show a similar tendency with variation in the Ni content. In the present work, there are two limitations, i.e. (1) experimentally, we did not confirm the exact percentage of Ni in $CsPbBr_3$ nanocrystals, (2) in the case of HHG measurements, we did not quantify the absolute conversion efficiency of harmonics yield and plasma density of nanocrystals. In our future work, it might be possible to address the above two limitations by quantifying plasma components in doped and Ni-doped $CsPbBr_3$ nanocrystals.

Acknowledgments

SRK special thanks to Dr Murali Banovath (Solar Cells and Photonics Research Laboratory, School of Chemistry), and Prof Soma Venugopal Rao (Advanced Center of Research in High Energy Materials), University of Hyderabad, Hyderabad 500046, Telangana, India, for providing the studied nanocrystals.

Data availability statement

The data that support the findings of this study are available upon reasonable request from the authors.

Funding

This work is funded by National Natural Science Foundation of China (Grant No. 62121005), the Chinese Academy of Sciences President's International Fellowship Initiative (2021PM0036, 2022VMA0012). The Innovation Grant of Changchun Institute of Optics, Fine Mechanics and Physics (CIOMP), Jilin Provincial Science and Technology Development Project (YDZJ202102CXJD002), Development Program of the Science and Technology of Jilin Province (20200802001GH). European Regional Development Fund (1.1.1.5/19/A/003).

Conflicts of interest

The authors declare no conflict of interest.

ORCID iDs

Srinivasa Rao Konda https://orcid.org/0000-0002-9001-4857
Rashid A Ganeev https://orcid.org/0000-0001-5522-1802
Vyacheslav V Kim https://orcid.org/0000-0001-5996-2296
Ravi Ketavath https://orcid.org/0000-0002-1853-9210
Jiaqi Yu https://orcid.org/0000-0002-9953-7873
Wei Li https://orcid.org/0000-0002-2227-9431

References

[1] Takahashi E J, Nabekawa Y and Midorikawa K 2004 *Appl. Phys. Lett.* **84** 4–6
[2] Takahashi E, Nabekawa Y, Otsuka T, Obara M and Midorikawa K 2002 *Phys. Rev.* A **66** 021802
[3] Constant E, Garzella D, Breger P, Mével E, Dorrer C, Le Blanc C, Salin F and Agostini P 1999 *Phys. Rev. Lett.* **82** 1668–71
[4] Ma R M and Oulton R F 2019 *Nat. Nanotechnol.* **14** 12–22
[5] Ahmadivand A and Gerislioglu B 2021 *Mater. Today* **51** 208–21
[6] Strelkov V 2010 *Phys. Rev. Lett.* **104** 26–9
[7] Rosenthal N and Marcus G 2015 *Phys. Rev. Lett.* **133901** 1–4
[8] Saleem M I, Yang S, Sulaman M, Hu J, Chandrasekar P V, Shi Y, Zhi R, Batool A and Zou B 2020 *Nanotechnology* **31** 165502
[9] Zhao A, Sheng Y, Liu C, Yuan S, Shan X, Di Y and Gan Z 2021 *Nanotechnology* **32** 135701
[10] Shu B, Chang Y, Xu E, Yang S and Zhang J 2021 *Nanotechnology* **32** 145712
[11] Yao Y, Hang P, Wang P, Xu L and Cui C 2020 *Nanotechnology* **31** 085401
[12] Luo Z *et al* 2016 *Nanoscale* **8** 1066–72

[13] Zhu H, Fu Y, Meng F, Wu X, Gong Z, Ding Q, Gustafsson M V, Trinh M T, Jin S and Zhu X Y 2015 *Nat. Mater.* **14** 636–42
[14] Kanemitsu Y and Handa T 2018 *Jpn. J. Appl. Phys.* **57** 90101
[15] Ravi V K, Swarnkar A, Chakraborty R and Nag A 2016 *Nanotechnology* **27** 325708
[16] Talbert E M *et al* 2016 *RSC Adv.* **6** 86947–54
[17] Kong W, Zhao C, Huang T, Li X, Xing J, Yu Z, Yang P, Li W and Yu W 2022 *ACS Appl. Mater. Interfaces* **14** 28154–62
[18] Krishnakanth K N, Seth S, Samanta A and Rao S V 2018 *Opt. Lett.* **43** 603–6
[19] Lin S, Lin H, Chen G, Wang B, Yue X, Huang Q, Xu J, Cheng Y and Wang Y 2021 *Laser Photon. Rev.* **15** 1–12
[20] Mo Q, Chen C, Cai W, Zhao S, Yan D and Zang Z 2021 *Laser Photon. Rev.* **15** 1–9
[21] Shen K C *et al* 2021 *Laser Photon. Rev.* **15** 1–10
[22] Li C, Zang Z, Han C, Hu Z, Tang X, Du J, Leng Y and Sun K 2017 *Nano Energy* **40** 195–202
[23] Yan D, Shi T, Zang Z, Zhou T, Liu Z, Zhang Z, Du J, Leng Y and Tang X 2019 *Small* **15** 1901173
[24] Yan D, Shi T, Zang Z, Zhao S, Du J and Leng Y 2020 *Chem. Eng. J.* **401** 126066
[25] Yan D, Zhao S, Zhang Y, Wang H and Zang Z 2022 *Opto-Electron. Adv.* **5** 1–14
[26] Pan G *et al* 2017 *Nano Lett.* **17** 8005–11
[27] Zhou S *et al* 2019 *ACS Energy Lett.* **4** 534–41
[28] Yong Z J *et al* 2018 *J. Am. Chem. Soc.* **140** 9942–51
[29] Ketavath R, Katturi N K, Ghugal S G, Kolli H K, Swetha T, Soma V R and Murali B 2019 *J. Phys. Chem. Lett.* **10** 5577–84
[30] Konda S R, Soma V R, Banavoth M, Ketavath R, Mottamchetty V, Lai Y H and Li W 2021 *ACS Appl. Nano Mater.* **4** 8292–301
[31] Konda S R, Soma V R, Ganeev R A, Banavoth M, Ketavath R and Li W 2022 *J. Mater. Sci.* **57** 3468–85
[32] Ganeev R A, Bom L B E, Wong M C H, Brichta J-P, Bhardwaj V R, Redkin P V and Ozaki T 2009 *Phys. Rev.* A **80** 043808
[33] Hutchison C, Ganeev R A, Witting T, Frank F, Okell W A, Tisch J W G and Marangos J P 2012 *Opt. Lett.* **37** 2064–6
[34] Maurya S K, Rout A, Ganeev R A and Guo C 2019 *J. Nanomater.* **2019** 968691312
[35] Konda S R, Lai Y H and Li W 2022 *Opt. Laser Technol.* **146** 107602
[36] Konda S R, Lai Y H and Li W 2021 *J. Appl. Phys.* **130** 013101
[37] Verhoff B, Harilal S S, Freeman J R, Diwakar P K and Hassanein A 2012 *J. Appl. Phys.* **112** 093303
[38] Mao S S, Mao X, Greif R and Russo R E 2000 *Appl. Phys. Lett.* **77** 2464–6
[39] Gurlui S, Agop M, Nica P, Ziskind M and Focsa C 2008 *Phys. Rev.* E **78** 1–9
[40] Hadrich S, Krebs M, Hoffmann A, Klenke A, Rothhardt J, Limpert J and Tu A 2015 *Light: Sci. Appl.* **4** e320
[41] Li J J, Lu J, Chew A, Han S, Li J J, Wu Y, Wang H, Ghimire S and Chang Z 2020 *Nat. Commun.* **11** 2748
[42] Kanda N, Imahoko T, Yoshida K, Tanabashi A, Amani Eilanlou A, Nabekawa Y, Sumiyoshi T, Kuwata-Gonokami M and Midorikawa K 2020 *Light: Sci. Appl.* **9** 168
[43] Chen Z and Segev M 2021 *eLight* **1** 1–12
[44] Sheik-Bahae M, Said A A, Wei T H, Hagan D J and Van Stryland E W 1990 *IEEE J. Quantum Electron.* **26** 760–9
[45] Liu X, Guo S, Wang H and Hou L 2001 *Opt. Commun.* **197** 431–7
[46] Kim V V, Ganeev R A, Konda S R, Boltaev G S, Sapaev I B, Yu W and Li W 2022 *Sci. Rep.* **12** 1–13
[47] Kim I J, Kim C M, Kim H T, Lee G H, Lee Y S, Park J Y, Cho D J and Nam C H 2005 *Phys. Rev. Lett.* **94** 243901
[48] Boltaev G S, Iqbal M, Abbasi N A, Kim V V, Ganeev R A and Alnaser A S 2021 *Sci. Rep.* **11** 1–11
[49] Ganeev R A and Kuroda H 2021 *Photonics* **8** 1–12
[50] Ganeev R A *et al* 2007 *Appl. Phys.* B **87** 243–7
[51] Ganeev R A, Suzuki M, Redkin P V, Baba M and Kuroda H 2007 *Phys. Rev.* A **76** 023832
[52] Corkum P B 1993 *Phys. Rev. Lett.* **71** 1994–7
[53] Priyadarshini M, Acharyya J N, Mahajan S and Vijaya Prakash G 2021 *Opt. Laser Technol.* **139** 107008
[54] Mondal K, Biswas S, Singha T, Pal S K, Datta P K, Ghosh S K and Kumbhakar P 2021 *Opt. Lett.* **46** 4879
[55] Lewenstein M, Balcou P, Ivanov M Y, Huillier A L and Corkum P B 1994 *Phys. Rev.* A **49** 2117–32